ADVANCED FUNCTIONAL MATERIALS
www.afm-journal.de

Auto-Pressurized Multi-Stage Tesla-Valve Type Microreactors in Carbon Monoliths Obtained Through 3D Printing: Impact of Design on Fluid Dynamics and Catalytic Activity

*Adriana Parra-Marfil, Carlos Gilberto Aguilar-Madera, Agustín Francisco Pérez-Cadenas, Francisco Carrasco-Marín, Saúl Omar Gutiérrez-Reina, Agustín Bueno-López, Raúl Ocampo-Pérez, and Esther Bailón-García**

The present research exploits an innovative methodology for producing auto-pressurized carbon microreactors with a precise and controlled structure analyzing the influence of their design on the fluid dynamics and their catalytic performance. Carbon monoliths with Tesla-valve shape channels (Tesla, T, and modified Tesla, Tm) are synthesized through the combination of 3D printing and sol–gel process and further probed as Ni/CeO2 supports on CO2 methanation. The experimental results and mathematical modeling corroborated the improved performance obtained through the complex design compared to a conventional one. In addition to chaotic fluid flow induced by the deviation in flow direction, which improves the reagents-active phase interaction, local pressure increases due to convergence of flows may enhance the Sabatier reaction according to Le Châtelier's principle. Conversely to straight channels, T and Tm are not affected by flow rate and presented chemical control. Tesla-valve with curved angle (Tm) improved the mass transfer, achieving higher conversion and ≈30% reaction rate increase regarding right angle (T). Thus, this auto-pressurized multi-stage Tesla-valve monolith opens the gate to design specific and advanced functional materials for multitude chemical reactions where not only the reactant-active phase contact can be maximized but also the reaction conditions can be controlled to maximize the reaction kinetics.

1. Introduction

CO_2 atmospheric levels, which account for ≈79% of greenhouse gas emissions, are steadily increasing due to human activities, mainly energy consumption.[1] This growth in emissions severely impacts the climate change, thus generating a crucial necessity to find and implement solutions to this problem. Among the major strategies considered so far, the use of carbon capture and sequestration technologies, and the energy transition from fossil fuel to more sustainable energy sources can be mentioned.[2,3] In this context, the valorization of CO_2 through its transformation into high-value fuels may not only help to mitigate environmental damage, but also to reduce the existing dependence on fossil fuels.[1,4–6] This valorization can be developed via its hydrogenation to methane (1), also called as CO_2 methanation reaction or Sabatier reaction.[7,8] The product obtained is chemically similar to natural

A. Parra-Marfil, A. F. Pérez-Cadenas, F. Carrasco-Marín, E. Bailón-García
Materiales Polifuncionales Basados en Carbono (UGR-Carbon)
Departamento Química Inorgánica – Unidad de Excelencia Química Aplicada a Biomedicina y Medioambiente – Universidad de Granada (UEQ-UGR)
Granada ES 18071, Spain
E-mail: estherbg@ugr.es

The ORCID identification number(s) for the author(s) of this article can be found under https://doi.org/10.1002/adfm.202403659

DOI: 10.1002/adfm.202403659

A. Parra-Marfil, S. O. Gutiérrez-Reina, R. Ocampo-Pérez
Centro de Investigación y Estudios de Posgrado (CIEP), Facultad de Ciencias Químicas
Universidad Autónoma de San Luis Potosí (FCQ-UASLP)
San Luis Potosí MX 78260, México

C. G. Aguilar-Madera
Facultad de Ciencias de la Tierra
Universidad Autónoma de Nuevo León (UANL)
Carretera a Cerro Prieto Km. 8 Ex Hacienda de Guadalupe, Linares MX 67700, México

A. Bueno-López
Departamento de Química Inorgánica
Universidad de Alicante (UA)
Alicante ES 03080, Spain

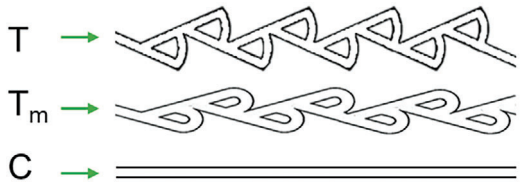

Figure 1. Structure design of channels: Tesla-valve type (T), modified Tesla-vale (Tm) and conventional honeycomb (C) monoliths.

gas, therefore can be straightly introduced into the natural gas infrastructure.[9,10–12]

$$CO_2 + 4H_2 \leftrightarrow CH_4 + 2H_2O, \Delta H_{298K} = -165\ \text{kJmol}^{-1} \quad (1)$$

Although the CO_2 methanation reaction is thermodynamically suitable at low temperatures, it is also kinetically limited owing to the chemical stability of the C=O bond of CO_2.[1,13–15] Hence, the development of selective, efficient, and stable catalysts that favor its dissociation is necessary for enhancing the reaction rate of CO_2 methanation at low temperatures. In that respect, several studies have been conducted on the production of supported catalysts usually composed of active metals, either noble (Rh, Ru, Pd, etc.) or non-noble (Co, Fe, Ni, Cu, etc.), which provide active sites for activation and dissociation of CO_2 and H_2.[4,11,16–27] Within the catalysts developed to date, Ni-based ones are the most studied and applied owing to the great activity and methane yields provided by Ni, presenting a considerably better cost-effectiveness ratio compared to noble metals.[15,28–31] Furthermore, the large amount of surface oxygen vacancies of CeO_2 facilitates the activation and dissociation of CO_2 and metal-support interaction, therefore, Ni/CeO_2 catalysts enhance low temperature performance of CO_2 methanation.[32–35]

On the other side, CO_2 methanation is a reversible and extremely exothermic reaction, thus resulting in temperature increase and hot spot formation.[36] This temperature increase may lead to carbon deposition and sintering, that is, catalyst deactivation. Therefore, besides the ability to transform the CO_2, catalyst configuration must help to handle and release the excessive heat generated from the exothermic reaction. This implies a defiance both in the temperature resistance and heat transfer properties.

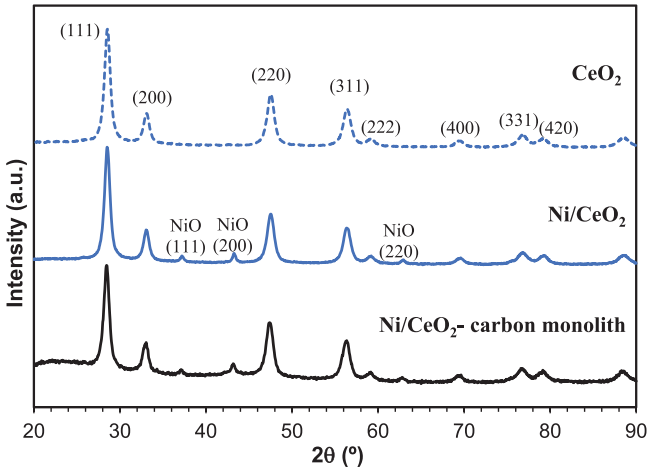

Figure 2. X-ray diffractograms of powdered CeO_2 and Ni/CeO_2, and Ni/CeO_2-coated carbon monolith.

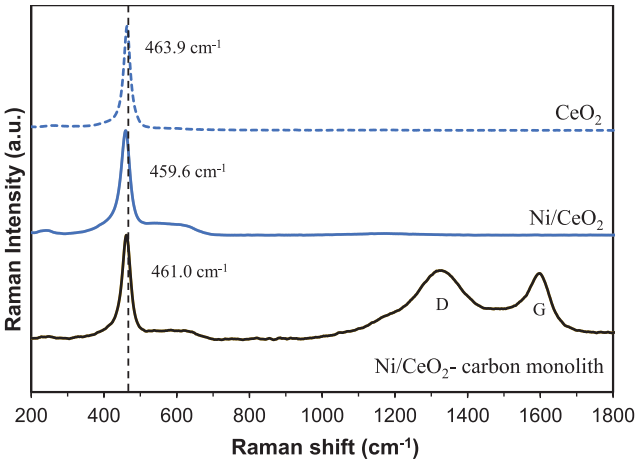

Figure 3. Raman spectra of powdered CeO_2 and Ni/CeO_2, and Ni/CeO_2-coated carbon monolith.

Macro structured supports such as monoliths and microchannel reactors have been studied and applied to overcome the problems commonly found in packed-bed reactors, mainly high pressure drop and heat and mass transfer limitations.[37,38] The better mass transfer between reagents flow and catalyst surface favors the reaction rate, while the heat transfer helps to prevent hot spots formation within the catalyst, as well as to avert approaching the chemical equilibrium disfavored at high temperatures that limits the methane yield.[38,39] Moreover, these structures can provide attractive advantages for their use in industrial scale, like high surface-to-volume ratios, no attrition, and easy separation process.[40]

Some authors have reported that conforming the Ni-based active phase for methanation into honeycomb monoliths increases its stability and activity due to the transport properties provided by this type of structures.[41,42] Ni/GDC (gadolinium-doped-ceria) was in situ deposited by solution combustion synthesis (SCS) on cordierite monoliths by Vita et al.[43] to use them as CO_2 methanation catalysts. The structured materials exhibited high methane productivity per unit weight of catalyst at 400 °C requiring low catalytic loading and allowing the treatment of large flow rates (Gas hourly space velocity, GHSV = 10 000–50 000 h^{-1}). Agueniou et al.[44] printed stainless steel honeycomb monoliths by selective laser sintering and washcoated them with Ni/CeO_2-ZrO_2 for the dry reforming of methane. Within the range of 750–900 °C the catalysts presented good activity with conversions around up to 95%. Additionally, the activation time generally required is avoided due to the improvement in heat transfer assistance. Structured NiFe-loaded ceramic catalysts exhibited good catalytic activity in CO_2 methanation, reaching up to 70% CO_2 conversion at 300 °C.[45] NiFe catalyst, originated from in situ grown layered double hydroxides, was precipitated on the exterior surface of cordierite monoliths previously coated with alumina or silica to increase its surface area. Catalyst coated with alumina

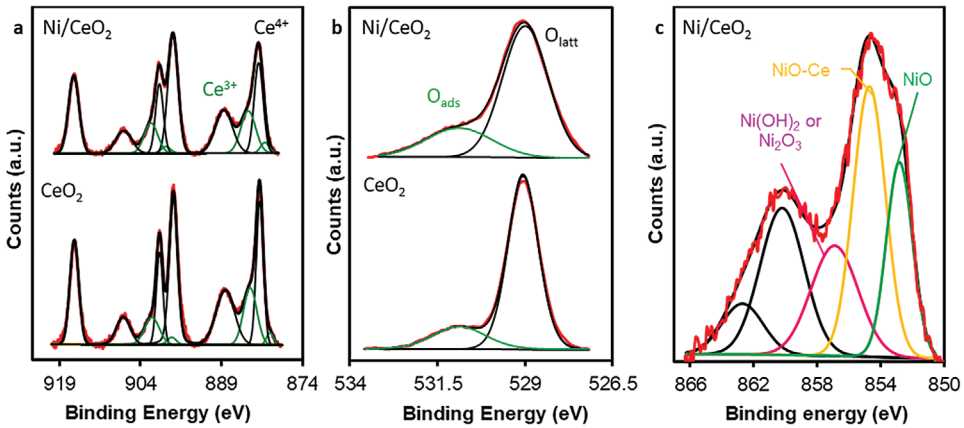

Figure 4. XPS results: a) Ce_{3d}, b) O_{1s} and c) $Ni_{2p3/2}$ regions.

exhibited greater CO_2 conversions than those with silica. This was associated to the deposition of NiFe into the channel wall, which in the case of silica washcoat loaded further inside compared to alumina one, thus resulting less accessible to the reagents flow due to the laminar flow imposed by the straight channel design.

Nonetheless, conventional straight channels force laminar flow creating radial diffusion limitations,[46–48] so non-straight channels which can generate turbulence, nonlinear streamlines, and local mixing of solutes within them due to tortuous paths would be desired to increase the active phase efficiency. Although 3D printing technology has recently surged as an alternative to overcome the limitations imposed by conventional synthesis methods, such as extrusion, pressing, or corrugating foil, to produce only straight channels, it has been barely studied for producing complex monolithic catalysts.[47–53] In this context, the monolithic catalysts studied so far in CO_2 methanation have been mainly produced with conventional shape from ceramic or metal raw materials, which implies some disadvantages such as the difficulty to incorporate the active phase with a homogeneous coat. In a previous study, we synthesized for the first time, pure and integral carbon monoliths with specifically and rigorously designed geometry and porous texture by combining the sol–gel polymerization of resorcinol and formaldehyde and the 3D printing technology.[50] The turbulent path created by the tortuous channels that split and join successively along the monolith, favors the active phase-gas contact and, even, the gas diffusion inside the macroporosity of the carbon skeleton improving the catalytic performance of the active phase with respect to the conventional honeycomb design.[50] Thus, we clearly demonstrate that 3D printing opens new design possibilities that outperform conventional catalysts.

In the present study, we go a step further and so, in addition to the control of the fluid dynamics, auto-pressurized microreactors could be created favoring the CO_2 methanation reaction by controlling the channel morphology. Thus, the aim is on creating a monolithic structure with a Tesla-valve type channels configuration for improving fluid flow and create auto-pressurized microreactors along the channel, while also attaining the textural properties and chemical stability of carbon. Considering this, two monoliths of different types of Tesla-valve channels are produced and washcoated with Ni/CeO_2 to evaluate their performance as catalysts in the Sabatier reaction. In addition, the present work develops a proper mathematical model to analyze the fluid dynamics, and to predict the velocity fluid profiles inside the channels of the catalytic structure.

2. Experimental Section

2.1. Catalyst Preparation

2.1.1. Active Phase Synthesis

A Ni/CeO_2 active phase had been prepared and used in this study. This active phase had been extensively tested in the previous studies, and had been selected for the current study of the novel catalyst supports because has high activity, selectivity and stability.[54]

CeO_2 was synthesized through the thermal decomposition of cerium nitrate hexahydrate ($Ce(NO_3)_3{\cdot}6H_2O$, ≥99.5% Alfa Aesar) via calcination at 500 °C in a muffle for 4 h. Subsequently, the CeO_2 was impregnated with an ethanolic solution of nickel (II) nitrate hexahydrate ($Ni(NO_3)_2{\cdot}6H_2O$, ≥97% Sigma–Aldrich) considering a 10 wt% of Ni and, finally, a calcination process at 600 °C for 5 h was followed for decomposing the nickel salt and obtain the Ni/CeO_2 active phase.

2.2. Carbon Supports Obtained Based on 3D Printing

Two monolithic carbon catalysts were produced with the advanced designs based on the Tesla-valve, Tesla (T) and modified Tesla (Tm), shown in **Figure 1**. Tesla-valve type channel is proposed to favor the turbulence and mass and heat transfer within the catalyst, and the impact of changing between right and curved angles in the valve (T and Tm, respectively) was evaluated in the CO_2 methanation performance. In order to synthesize this complex carbon structures, non-attainable through conventional methods, a methodology combining 3D printing and sol–gel process is conducted. The designs, which served as negative of the

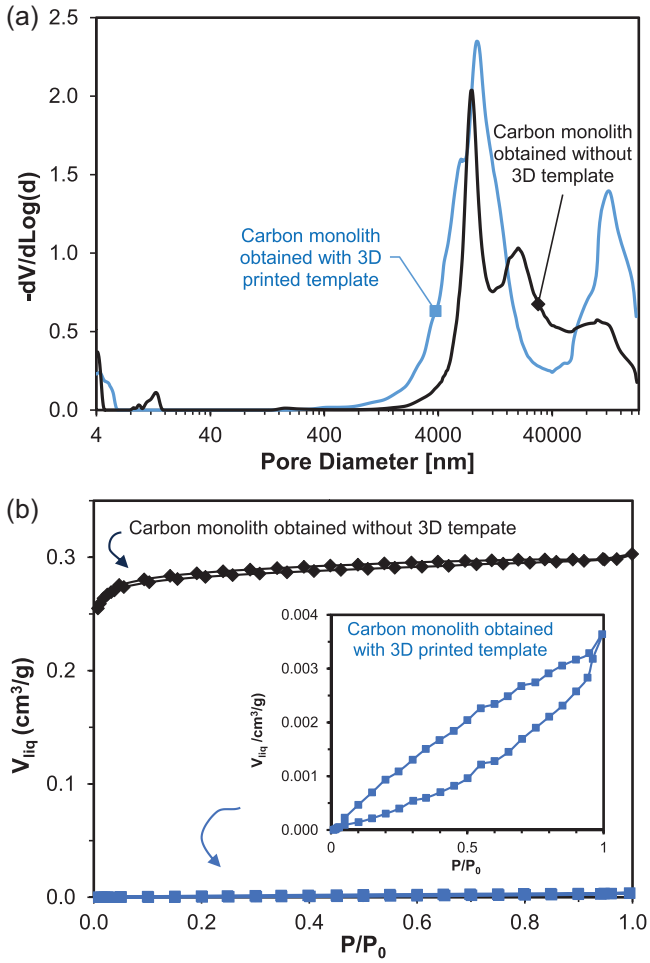

Figure 5. a) Pore size distributions determined by mercury intrusion porosimetry, and b) N_2 adsorption–desorption isotherms at −196 °C of a reference carbon monolith (without template) and a carbon monolith prepared using a 3D printed template.

desired channels, were obtained with Cubify Invent software, and then used in an Ultimaker^{2+} 3D printer to print polymeric templates. A conventional honeycomb carbon monolith with straight channels (C) was also obtained and used as reference.

After the template was printed, a carbon precursor solution was prepared consisting of resorcinol (R), formaldehyde (F), and water (W) with R/F and R/W molar ratios of 1/2 and 1/15, correspondingly. Afterward, the templates were introduced in glass tubes (≈2.7 cm internal diameter) and later filled with the R/F/W solution and sealed. Then, a controlled polymerization process was conducted as follows: 1 day at room temperature, 1 day at 50 °C, and 5 days at 80 °C. Once completed, the organic monoliths obtained were demolded and immersed in acetone for 3 days to exchange the water within the structure, aiding the drying process and minimizing pore damage. Finally, the dried organic monoliths were carbonized at 850 °C for 2 h with a heating rate of 1.5 °C min^{-1}. The resulting monoliths presented an ≈20% shrinkage, with final dimensions of ≈2.15 cm diameter and 3.5 cm length. the total volume of the monoliths is 12.7 mL, of which ≈2.5 mL correspond to the channels' volume.

2.3. Active Phase Loading

The previously prepared Ni/CeO_2 active phase was loaded onto the carbon monoliths through dip-coating. Carbon monoliths were immersed in an ethanolic suspension containing Ni/CeO_2 at 10 wt%. Subsequently, the monoliths were horizontally rotated during 24 h at room temperature to ensure a uniform distribution, and then they were dried overnight at 80 °C. Any excess of active phase not firmly attached to the monolith surface, which could potentially block the channels, was removed using compressed air. The loading of Ni/CeO_2 was confirmed by observing the weight difference of the dried monoliths after each impregnation. This process was repeated until a loading of 800 ± 5 mg per monolith was achieved.

2.4. Catalyst Characterization

To obtain data on the surface area of the carbon structure, adsorption isotherms (N_2 at −196 °C and CO_2 at 0 °C) were acquired by means of a Quantachrome Autosorb-6B instrument. Before the gas adsorption assessments, the samples underwent a degassing process at 110 °C for 8 h. Besides, Hg-porosimetry was also utilized to study the textural properties. The samples were previously degassed at 50 °C for 12 h, and the analysis was effectuated through a Poremaster 60 GT (Quantachrome) equipment from an initial pressure of 7 KPa up to 390 000 KPa. The contact angle and surface tension used for pore size calculations were $\theta = 140$ ° and $\gamma = 480$ dyn cm^{-1}, respectively.

The surface chemistry of the CeO_2 support and the active phase Ni/CeO_2 was analyzed through X-ray photoelectron spectroscopy (XPS). A K-ALPHA Thermo Scientific device with an X-ray source Al-Kα radiation at 1486.6 eV was used. Furthermore, the crystalline structure of the catalyst and the effect of loading onto a carbon monolith were examined through X-ray diffraction (XRD) and Raman spectroscopy. A Bruker D8 DISCOVER X-Ray diffractometer with CuKα-ray radiation ($\lambda = 1.5418$ Å) was used to obtain the XRD patterns within the 2θ range of 10–90°

Table 1. Textural characterization of carbon monoliths.

Sample	N_2 adsorption			CO_2 adsorption		Hg-porosimetry	
	S_{BET} [m²/g]	V_{N2} [cm³/g]	L_0 [nm]	V_{CO2} [cm³/g]	L_0 [nm]	V_{meso} [cm³/g]	V_{macro} [cm³/g]
Monolith without template	639	0.29	0.67	0.31	0.61	0.04	0.90
Monolith with template	2	0	–	0.34	0.79	0.04	1.23

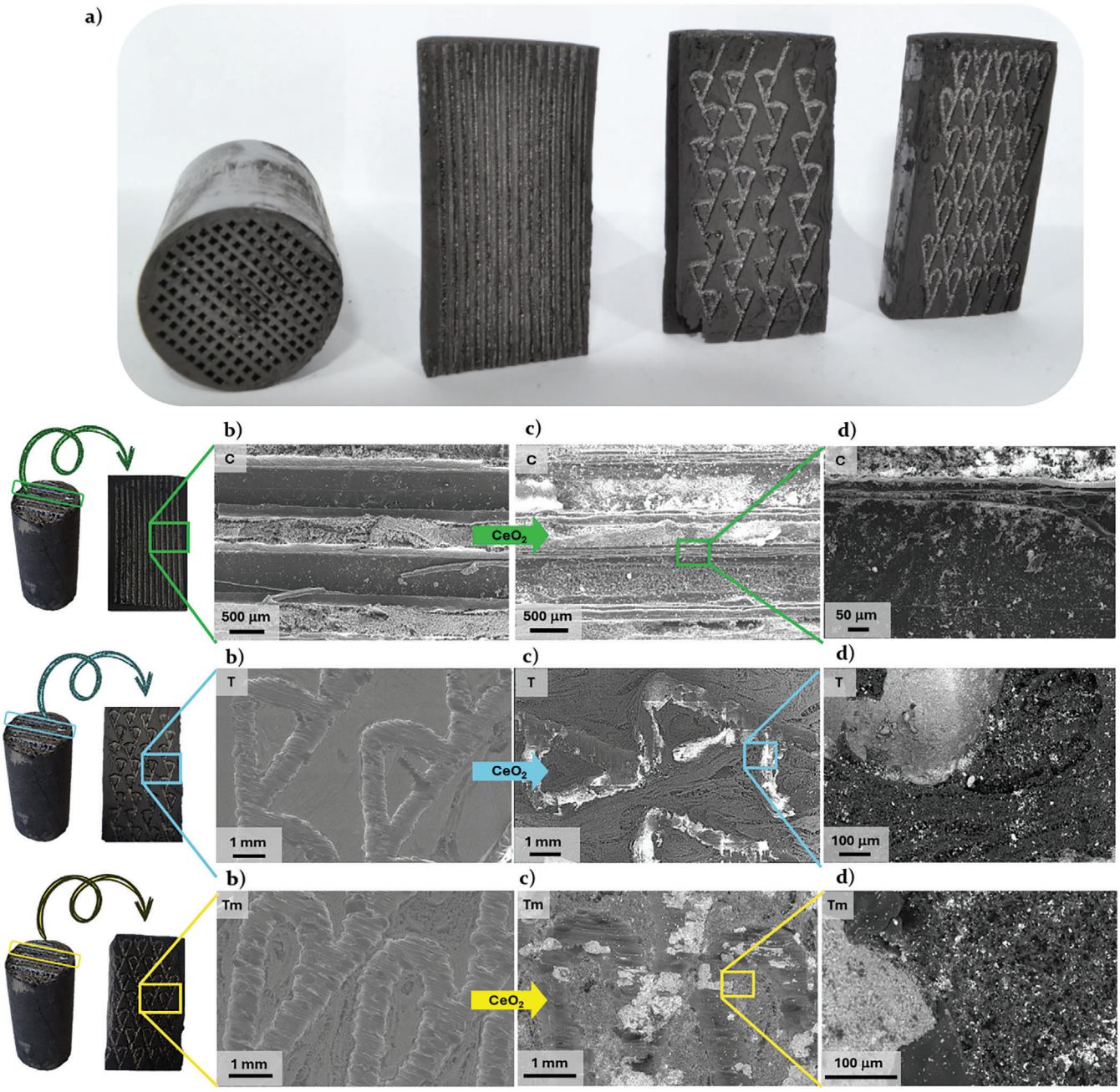

Figure 6. Images and SEM micrographs of C, T, and Tm carbon monoliths: a) structure of the monolith; b) channel morphology, c) Ni/CeO_2-impregnated monolith and d) magnification of the channel/wall interface showing the Ni/CeO_2 active phase distribution on the carbon matrix and the channel.

at 1° min^{-1}. Raman analysis was performed using a Jasco NRS-5100 dispersive micro-Raman microscope equipped with a Green Diode (532 nm, 30 mW, Elforlight G4-30; Nd:YAG).

Scanning electron microscopy (SEM) was employed to investigate the distribution of the active phase on the channels and carbon matrix of monolithic structures using a Zeiss SUPRA40VP Variable Pressure Scanning Electron Microscope (VP-FESEM) equipped with an EDX detector X-max 50. Additionally, thermal and mechanical properties were also determined. The thermal stability of the catalysts in oxidizing atmosphere was assessed by thermogravimetric analysis (TGA). Bare and coated monoliths were analyzed using a SDT 2960 DSC-TGA equipment, heating at 10 °C per min up to 900 °C under air flow. Mechanical properties were evaluated by means of compression tests and compared with a commercial cordierite honeycomb monolith. The monolithic samples were cut into 1.5 cm high cylinders, and the bases were sanded for smooth surfaces. Tests were conducted using a Shimadzu AGS-J 10 kN instrument with a constant approach speed of 1 mm min^{-1} and the compression test direction was top to bottom.

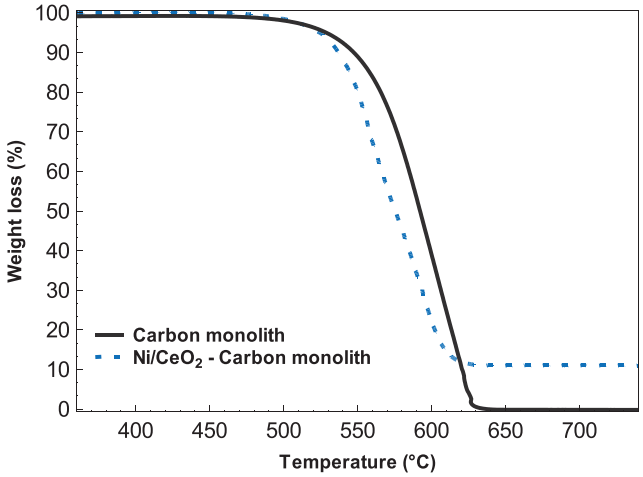

Figure 7. Thermogravimetric analysis in air of carbon monolith (T) and Ni/CeO_2-loaded carbon monolith (T).

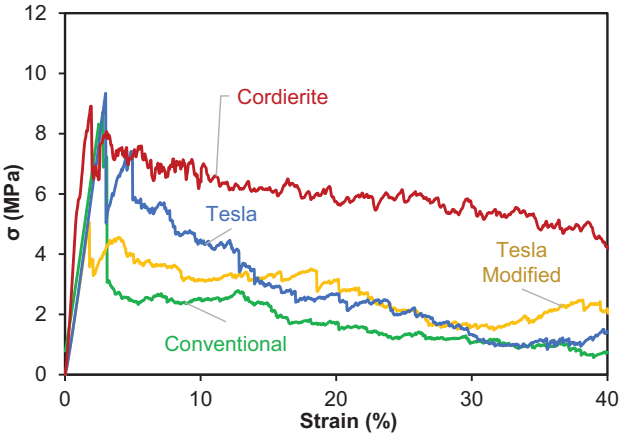

Figure 8. Comparison of the stress-strain curves obtained from carbon monoliths with tesla design (T), the modified tesla design (Tm), conventional design (C), and a reference commercial cordierite monolith of conventional honeycomb design.

2.5. Catalytic Tests

The catalysts performance and the impact of geometric modification were studied in the CO_2 methanation reaction. The experimental setup comprised placing a monolith in a quartz cylindrical reactor within a temperature-controlled furnace. To collect the produced water, a cold trap was integrated at the reactor's outlet, and the outflow (CO_2 and CH_4 gases) was analyzed using infrared gas sensors (Edinburgh Instruments LTD 034/00700). Before each experiment, the monolith under evaluation was subjected to treatment in a reducing atmosphere (10% H_2/Ar) at 500 °C for 1.5 h. Subsequently, the system was allowed to cool to 150 °C, and the inlet flow was switched to the reaction gas mixture (10% CO_2 and 40% H_2 balanced in Ar) with total flows varying from 100 to 500 mL min^{-1}. The temperature was incremented in 25 °C steps, with each temperature held for 20 min, reaching up to 450 °C. CO_2 conversion and selectivity to CH_4 were calculated to evaluate the catalytic performance.

2.6. Mathematical Model

The experimental data was introduced into a mathematical model that incorporates mass and momentum balances for the gas mixture of CO_2 methanation. The mathematical model incorporates four partial differential equations governing the momentum balance, the turbulent kinetic energy balance, the rate of dissipation of turbulent kinetic energy, and the gas-phase mass balance. The $\kappa - \epsilon$ mathematical model for momentum balance was applied, which was able to simulate turbulence within the monolith.

Table 2. Maximum compressive stress (σ_{max}) and Young's modulus (E) of the monoliths.

Sample	$\sigma_{máx}$ MPa	E Pa
T	9.34	3.20
T_m	5.04	2.93
C	9.15	3.10
Cordierite	9.0	1.90

The momentum balance is given by:

$$\rho\frac{\partial \boldsymbol{u}}{\partial t} + \rho(\boldsymbol{u}\cdot\nabla)\boldsymbol{u} = -\nabla p + \nabla\cdot\boldsymbol{K} \quad (2)$$

With,

$$\boldsymbol{K} = (\mu + \mu_T)\left[\nabla\boldsymbol{u} + (\nabla\boldsymbol{u})^T\right] \quad (3)$$

Here μ_T is the turbulent viscosity which is computed as follows:

$$\mu_T = \rho C_\mu \frac{\kappa^2}{\epsilon} \quad (4)$$

The turbulent kinetic energy κ obeys the following partial differential equation:

$$\rho\frac{\partial \kappa}{\partial t} + \rho(\boldsymbol{u}\cdot\nabla)\kappa = \nabla\cdot\left[\left(\mu + \mu_T\frac{\mu_T}{\sigma_\kappa}\right)\nabla\kappa\right] + P_\kappa - \rho\epsilon \quad (5)$$

While the rate of dissipation of turbulent kinetic energy is given by:

$$\rho\frac{\partial \epsilon}{\partial t} + \rho(\boldsymbol{u}\cdot\nabla)\epsilon = \nabla\cdot\left[\left(\mu + \mu_T\frac{\mu_T}{\sigma_\epsilon}\right)\nabla\epsilon\right] + C_{\epsilon1}\frac{\epsilon}{\kappa}P_\kappa - C_{\epsilon2}\rho\frac{\epsilon^2}{\kappa} \quad (6)$$

The term associated to the rate of deformation is defined as:

$$P_\kappa = \mu_T\left\{\nabla\boldsymbol{u} : \left[\nabla\boldsymbol{u} + (\nabla\boldsymbol{u})^T\right]\right\} \quad (7)$$

In addition, $\boldsymbol{\rho}$ represents the fluid mass density, $\boldsymbol{u}$ is the vector of velocity, t is the time, p is the pressure, and $\boldsymbol{\mu}$ is the fluid viscosity. The gas-phase mass balance is given by the continuity equation written as:

$$\frac{\partial \rho}{\partial t} + \nabla\cdot(\rho\boldsymbol{u}) = 0 \quad (8)$$

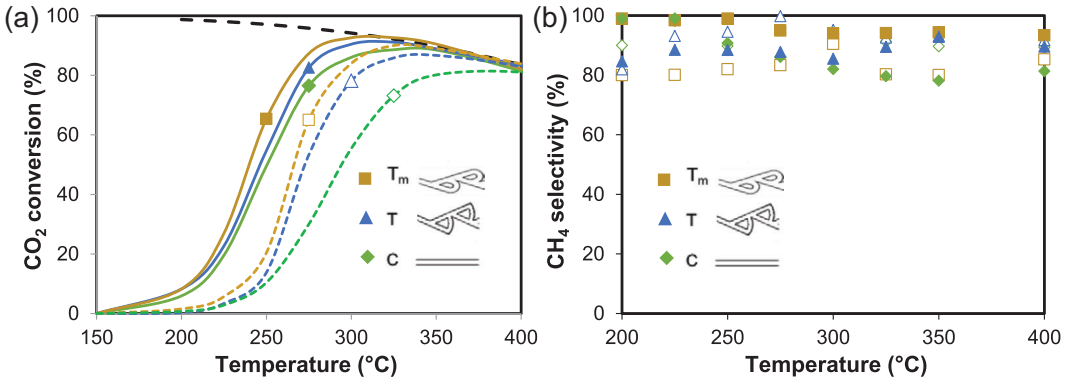

Figure 9. a) Conversion of CO_2 and b) selectivity to CH_4 of the Ni/CeO_2 active phase supported on carbon monoliths prepared with different channel architecture. Gas flow of 100 mL min^{-1} (continuous line) and 500 mL min^{-1} (dashed line).

The initial values of the pressure and velocity used to solve numerically the model are considered as:

$$\text{At } t = 0 \text{ min } \boldsymbol{u} = 0 \text{ m/s}, \; p = 1 \text{ atm} \tag{9}$$

Further, boundary conditions were stated at the inlet and outlet of the monolith. For the inlet boundary, the velocity is determined as:

$$-\boldsymbol{n} \cdot \boldsymbol{u} = u^{in} \tag{10}$$

Where $\boldsymbol{n}$ is the unit normal vector pointing outward the inlet boundary. The inlet velocity u^{in} is computed through the flow area and volumetric flow rate as follows:

$$u^{in} = Q/A \tag{11}$$

Whereas, at the outlet boundary the pressure is fixed:

$$p = 1\text{atm} \tag{12}$$

The nonslip and impenetrability conditions are enforced for the velocity vector at the monolith surface, $\boldsymbol{u} = 0$.

3. Results and Discussion

3.1. Characterization

3.1.1. Characterization of Active Phase

The crystal structure of Ni/CeO_2 active phase, both powdered and loaded onto the carbon monoliths, was analyzed by X-ray diffraction with the findings presented in **Figure 2**. Characteristic peaks corresponding to the fluorite face-centered cubic (FCC) crystalline structure of ceria (JCPDS 034–0394) at 28.5, 33.1, 47.6, and 56.5°, representing the (111), (200), (220), and (311) planes,[55–57] were presented in the X-ray diffractograms of all samples (Figure 2). In the case of the Ni/CeO_2 diffractogram, small peaks at 37.2, 43.2, and 63° were observed attributed to the (111), (200), and (220) crystallographic planes of the FCC structure of NiO (JCPDS 047–1049).[58]

The CeO_2 lattice parameter was estimated based on the XRD data, obtaining 0.5411 nm, consistent with that stated in JCPDS 00-034-0394. Note that CeO_2 peaks are slightly displaced in Ni/CeO_2 active phase, which is also manifested in the increase of the lattice parameter of CeO_2 (0.5420 and 0.5429 for unsupported and supported Ni/CeO_2, respectively). This change in the lattice parameter suggests that some nickel cations were introduced into the crystal lattice. Crystal sizes for CeO_2 and Ni/CeO_2 were determined using the Scherrer equation. The incorporation of nickel did not lead to a considerable change in the average size of the ceria crystals, as results were comparable for both pure CeO_2 (10.5 nm) and Ni/CeO_2 active phase (11.0 nm). Furthermore, it is important to highlight that the diffractogram of the Ni/CeO_2-coated monolith did not exhibit any notable change compared to the powdered active phase. This suggests that the coating process and the interaction between carbon structure and Ni/CeO_2 do not alter its crystalline characteristics.

Figure 3 shows the Raman spectra of bare ceria and the Ni/CeO_2 active phase both unsupported and supported on carbon monolith. The bare ceria presented a single band centered at 463.9 cm^{-1}, corresponding to the F_{2g} vibrational mode of the crystalline fluorite-type structure of ceria.[59] This intense peak is associated with symmetric Ce-O_8 stretching vibrations.[60,61] Owing to the presence of nickel and its interaction with ceria, the F_{2g} peak shifted to 459.5 cm^{-1} in the spectra of Ni/CeO_2 active phase confirming the insertion of Ni cations onto the ceria lattice observed by XRD. Further, a small shoulder emerges between 500 and 660 cm^{-1}, which is assigned to oxygen vacancies located at interfacial sites between Ni and CeO_2. In the Ni/CeO_2-coated carbon monolith, two new bands are observed at 1332 and 1599 cm^{-1} attributed to the D and G band of carbon, respectively. Note that both XRD and Raman data confirm that differences in ceria-related peaks are not observed between unsupported and supported on carbon monolith Ni/CeO_2 active phase, suggesting that the chemical nature of Ni/CeO_2 active phase is not alter by the coating process and anchoring on the carbon monolith surface. Therefore, the different catalytic performance of monoliths with different design should be ascribed to differences in the fluid dynamic behavior of the monolith and not to differences on the catalytic active phase.

The surface chemistry of the CeO_2 support and Ni/CeO_2 active phase was analyzed by XPS. Ce_{3d}, O_{1s} and Ni_{2p} XPS

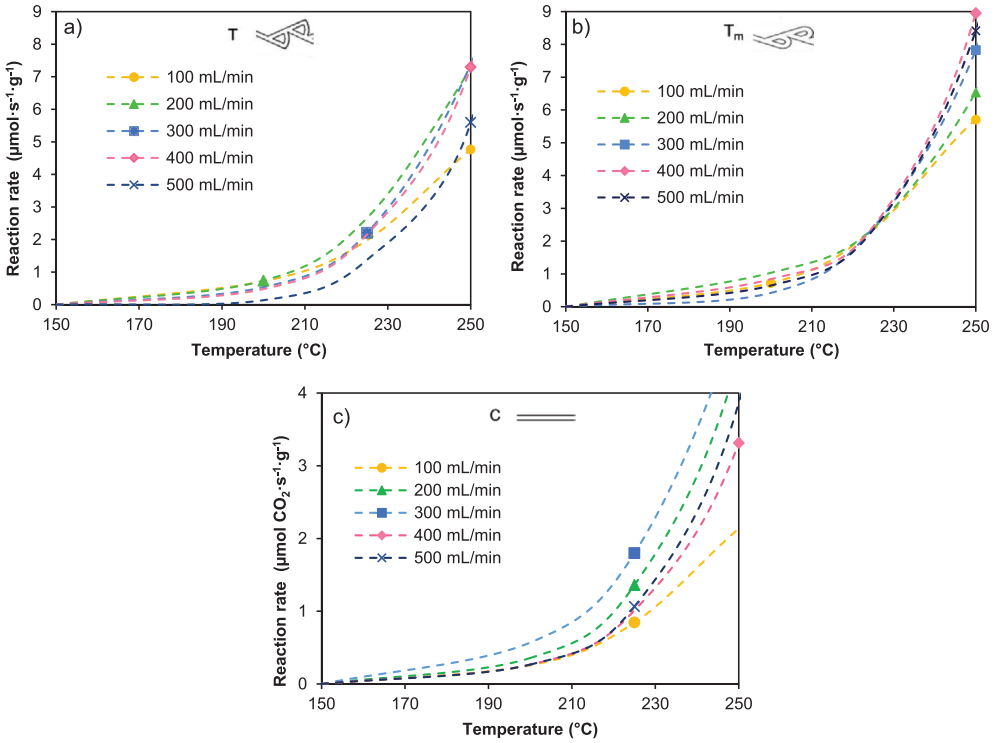

Figure 10. Reaction rate normalized by weight of Ni/CeO_2 supported on carbon monolithic catalysts: a) Tesla design; b) modified Tesla design and c) conventional design.

spectral regions are shown in **Figure 4**. Five doublets are required to deconvolve the Ce_{3d} region (Figure 4a). The peaks pairs at 882.0-900.3 eV, 888.2–907.0 eV, 898.0–916.3 are attributed to Ce^{4+} whereas the peaks at 880.3–898.6 eV and 884.0–902.3 eV are assigned to Ce^{3+}. The proportion of Ce^{3+} detected by XPS must be related with the reducibility of the surface.[62] Note that the reducibility of the surface is improved by the addition of Ni, mainly if this Ni is incorporated during the synthesis due to the higher dispersion and Ce-Ni contact in this case. Consequently, it is expected that the amount of Ce^{3+} detected by XPS increases in Ni/CeO_2 active phase regarding CeO_2 support. The surface Ce^{3+} content obtained by XPS was 18.9 and 22.5% for CeO_2 and Ni/CeO_2, respectively, due to the improved surface reducibility, which confirms the successful synthesis of Ni/CeO_2. This effect must also be observed in the O_{1s} region. The O_{1s} region requires two peaks for deconvolution (see Figure 4b): one peak centered at 529.0 eV, associated with surface lattice oxygen (O_{latt}), and another peak centered at 531.0 eV, attributed to adsorbed oxygen species (O_{ads}). Typically, O_{ads} species are present at oxygen vacancies, so a higher concentration of O_{ads} species suggests a greater population of oxygen vacancies. Therefore, the ratio of surface O_{ads} to O_{latt} can serve as an indicator of surface reducibility. The O_{ads}/O_{latt} ratio was 0.22 and 0.32 for CeO_2 and Ni/CeO_2, respectively indicating that Ni improves the surface ceria reducibility. Finally, the $Ni_{2p3/2}$ region of active phase was depicted in Figure 4c. In this spectral region, a primary band is observed within the 851–859 eV range, accompanied by a satellite structure at higher binding energies (859–866 eV). To deconvolute the $Ni_{2p3/2}$ region, three peaks are necessary, occurring ≈853.2, 855.0, and 857.2 eV. These peaks correspond to surface Ni^{2+} species within the NiO structure (surface NiO species), Ni^{2+} species closely associated with the ceria surface (NiO-Ce species), and Ni^{3+} or $Ni(OH)_2$ species, respectively.[62,63]

3.1.2. Characterization of Carbon Supports

Carbon monoliths with three different channel designs were synthesized combining the 3D printing of polymeric templates and the RF sol–gel polymerization. A monolith without template was also synthesized in order to analyze the influence of the polymeric template on the textural properties of the carbon monoliths. The textural properties were analyzed by N_2 and CO_2 adsorption at −196 °C and 0 °C, respectively, and Hg-porosimetry. Data were collected in **Figure 5** and **Table 1**. A type I isotherm, characteristic of microporous materials, was obtained for the carbon monolith synthesized without template. A slight N_2 uptake is observed at intermediate relative pressures manifesting the presence of some mesoporosity. CO_2 adsorption offers insights into the narrow microporosity, specifically micropores with a diameter less than 0.7 nm. The assessment of total

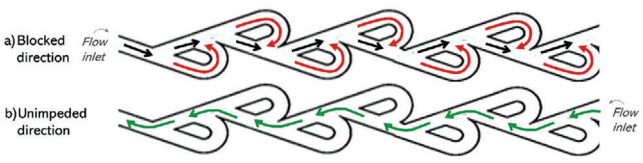

Figure 11. Principle of operation of a Tesla valve. a) blocked direction and b) unimpeded direction.

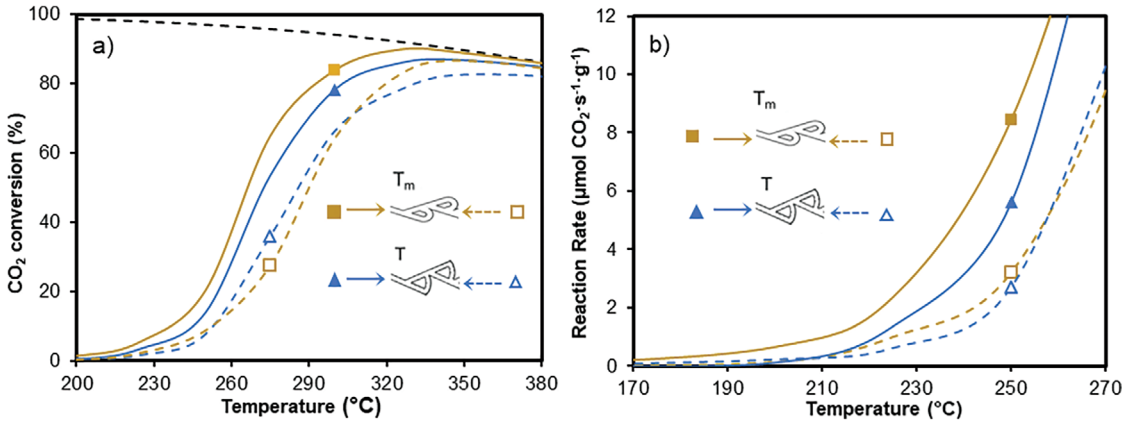

Figure 12. Comparison of catalytic performance of Tesla (T) and modified Tesla (Tm) design monoliths in the blocked direction (continuous line) and unimpeded direction (dashed line). a) CO_2 conversion and b) reaction rate normalized by weight of Ni/CeO_2 supported. Inlet volumetric flow of 500 mL min^{-1}.

microporosity is reliant on the N_2 isotherm, but only in the absence of diffusion restrictions.[64] Note that the micropores volume determined by CO_2 adsorption ($V_{CO2)}$ is greater than the micropores volume determined by N_2 adsorption V_{N2} (Table 1), indicating the prevalence of narrow micropores and thus certain N_2 diffusional restrictions into the microporosity induced by such narrow microporosity.

The use of the template provokes a huge decrease of the N_2 adsorption of the carbon monolith. A Type II N_2-adsorption isotherm (Figure 5b, **inlet**) was obtained for the monolith with template, characteristic of non-porous or macroporous adsorbents. A practically total blockage of microporosity is observed, whereas the narrow microporosity even increases with the use of template (V_{CO2}, Table 1). Thus, this wider porosity blockage could be ascribed to the effect of the polymeric template. During the final carbonization, the thermofusible polymer occupying the channels melts at low temperatures and fills the wider porosity (macro and mesoporosity) that was designed in the organic gel, leaving the channel with the desired geometry open. As the temperature increases, the organic RF matrix, along with the polymeric material, undergoes carbonization, obtaining the carbon monolith and removing the template. During this carbonization process, similar to what occurs in carbon molecular sieves prepared from an activated carbon by pitch pyrolysis,[65] part of the gases evolved during the polymer heat treatment, after cracking, are deposited in the porosity entrance, blocking partially the porosity existing in the carbon matrix creating a high number of ultra micropores characteristic of molecular sieves.

Hg-porosimetry (Figure 5a and Table 1) gives information about the wider porosity (mesopores and macropores). Note that highly opened macropores are mainly observed in both samples with a very low amount of mesopores (V_{meso}, Table 1). Three peaks centered at 8, 21, and 100 µm are observed in the Pore Size Distribution (PSD) of the carbon monolith obtained without template which are ascribed to the interparticle spaces leaved by the carbon gels clusters and some monolith cracks, respectively. However, the monolith obtained with the 3D printed template presents peaks centered at 6, 9 and 128 µm attributed to the filling of interparticle void of the carbon matrix and the channels, respectively. It is important to highlight that the peak ascribed to the carbon matrix voids becomes wider and shifts to lower pore diameter (Figure 5). This carbon matrix porosity narrowing could be ascribed to the deposition of carbon residues from the template.

This wide macroporosity, the channel morphology, and the Ni/CeO_2 distribution on the carbon surface were analyzed by SEM. Images are collected in **Figure 6**. A perfect replica of the channel template was obtained for the three channel designs. Note that even the layer-by-layer architecture of the fused deposition 3D-printed template is reproduced (Figure 6b). After the impregnation of the active phase (Figure 6c), the Ni/CeO_2 is distributed both along the channels and the wall

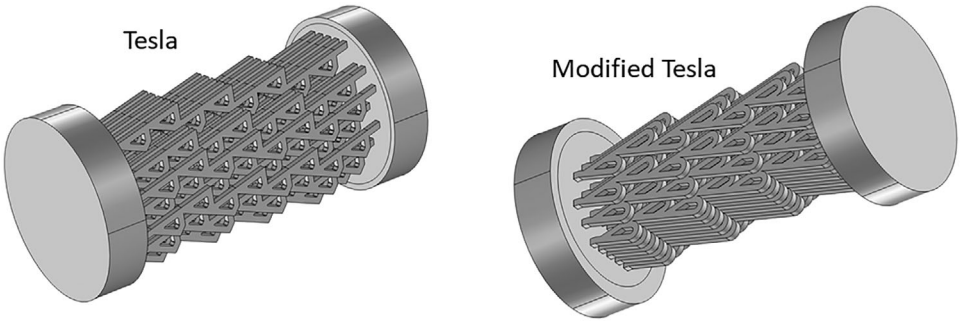

Figure 13. CAD design of the Tesla and modified Tesla monoliths in the Comsol Multiphysics environment.

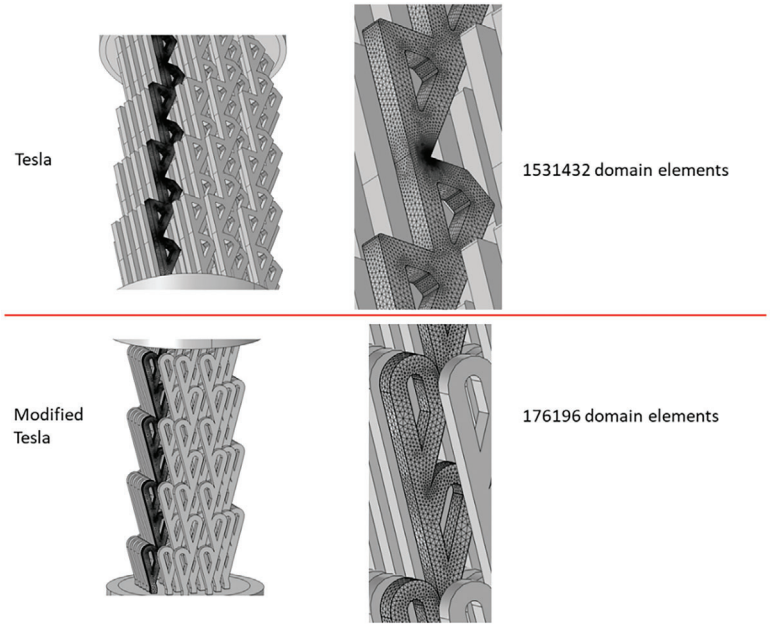

Figure 14. Discretization of the Tesla monoliths into multiple tetrahedra and pyramids as grid mesh subdomains.

carbon matrix. The magnification of the channel/wall interface (Figure 6d) shows that a huge part of the active phase is homogeneously distributed along the carbon matrix independently of the monolith design. This enhanced distribution along the carbon matrix is favored by the highly opened macroporosity of the carbon gels. SEM images of the carbon matrix (Figure S1, Supporting Information) manifests a sponge-like structure with pore of several µm as it was also pointed out by Hg-porosimetry. This opened macroporosity favors the diffusion of the ethanolic Ni/CeO_2 suspension and is wider enough to host particles of several tens of nm of the Ni/CeO_2 active phase.

The thermal stability of the bare and Ni/CeO_2-impregnated 3D-printed monoliths was analyzed by TGA using the T (Tesla-valve type) design (**Figure 7**). Both the impregnated and bare carbon monoliths are stable up to 500 °C under oxidizing atmosphere. At higher temperatures, the monoliths start to burn being completely burned at a temperature of ≈630 and 620 °C for the bare and impregnated monoliths, respectively. The presence of Ni/CeO_2, a well-known active phase for oxidizing reactions, favors the carbon phase burning off but the stability is still high to be used in reactions in which temperatures lower than 500 °C in oxidizing atmosphere are required. In the case of CO_2 methanation, the maximum temperature used is 450 °C under He atmosphere, so the stability of the carbon matrix is guaranteed.

The mechanical properties of the monoliths were also studied by means of compression tests and compared with a commercial cordierite honeycomb monolith. From the stress-strain curves (**Figure 8**), it is observed that the design does not highly affect the mechanical properties of the carbon monolith. At the beginning of the compression test, a linear relationship between strength and deformation indicates an elastic deformation. Once achieved the maximum stress resistance (σ_{max}), stress reduction is not as pronounced as occur in polymeric materials, indicating that the damage in both ceramic and carbon monoliths results from the gradual crushing of layers at the extremities. Note that the Tesla-valve type carbon monolith shows similar mechanical

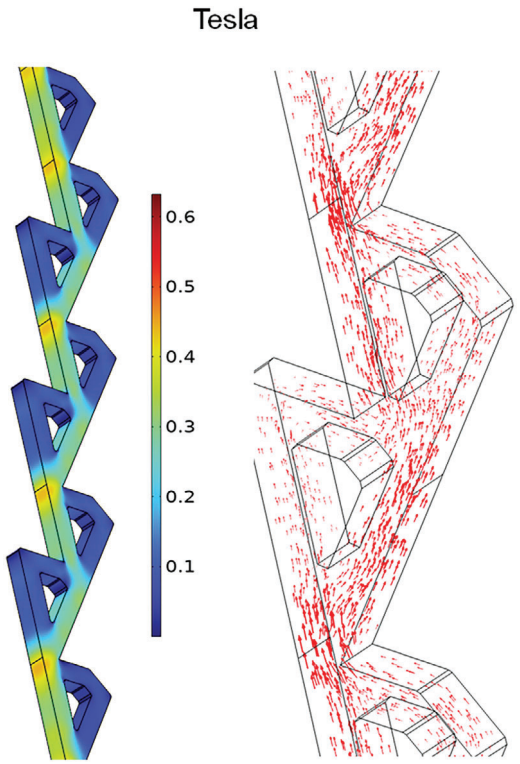

Figure 15. Magnitude of the fluid velocity (m s^{-1}) inside one channel of the Tesla monolith (left image), and the fluid direction (right image). Gas flow rate = 500 mL min^{-1}.

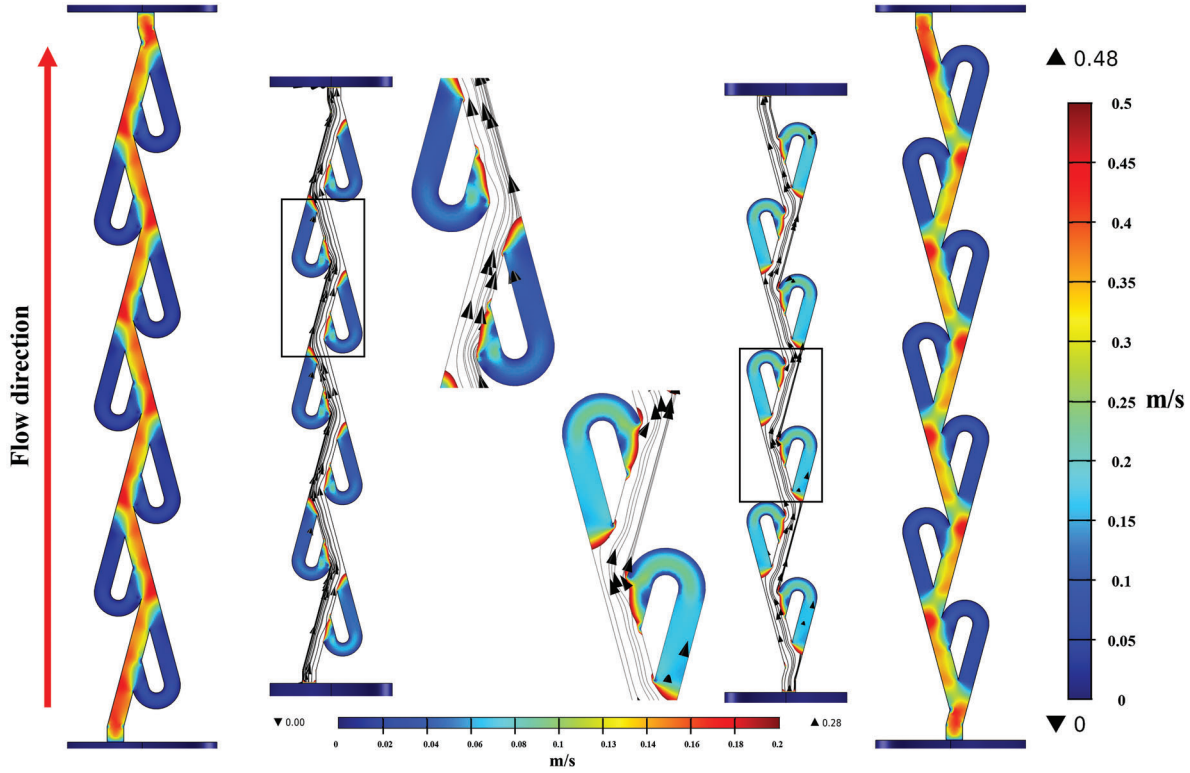

Figure 16. The magnitude of the fluid velocity inside one channel of the modified Tesla monolith. The black arrows show the main flow paths of the gaseous mixture. Gas flow rate = 500 mL min^{-1}.

properties than the cordierite one, being the yield points 9.34 and 9.0 MPa (**Table 2**), respectively. Therefore, carbon monoliths are stronger enough to be used as monolithic supports in industrial applications where cordierite monoliths are usually used.

3.2. Catalytic Results

The catalytic performance of the Ni/CeO_2-impregnated carbon monoliths was studied in the methanation of CO_2. To allow the comparison of the catalytic performance of carbon monoliths with different channel designs, a similar Ni/CeO_2 load was supported on all carbon monoliths (800 ± 5 mg). The variation of the CO_2 conversion and CH_4 selectivity with temperature for carbon monoliths prepared with different channels architectures is plotted in **Figure 9** for flow rates of 100 (continuous lines) and 500 mL min^{-1} (dashed lines). In all cases, as expected for Ni/CeO_2 active phase, the CH_4 selectivity is always higher than 80% (Figure 9b). However, note that the channel architecture influences the catalytic activity of the active phase (Figure 9a). The turbulence created by the Tesla-valve type channel configurations (T and Tm) enhances the reactants-active phase contact regarding the straight channeled design (C) improving mass and heat transfer within the catalyst and so, the catalytic performance. Tesla-valve structure has exceptional one-directional flow characteristics, either in forward or reverse flow direction, which selection under the same inlet pressure may affect the performance of the valve.[66,67] Several studies have shown that, due to its complex design, the reverse flow direction, or blocking direction, in the Tesla-valve causes the fluid to follow highly chaotic trajectories, prompted by the flow direction swerving.[68] This chaotic flow favors turbulence, leading to improved mixing, a higher interaction between the fluid and the structure, as well as an enhanced mass and heat transfer.[67–69] Furthermore, as the fluid bifurcates and later converges, the flow impingement at Tesla-valve junctions results in increased velocity and a certain amount of pressure drop.[69–72] However, local increases in pressure may also occur due to the obstruction and convergence of flows. In line with Le Châtelier's principle,[73–75] and considering the characteristics of Sabatier reaction, these pressure points may boost the CH_4 production. The change of the Tesla-valve angle from right (T) to curved angle (Tm) also improves the catalytic performance due to a better fluid dynamic of gases in Tm which allows a better mass and heat transfer as will be analyzed in the next section.

It is important to highlight that this catalytic activity enhancement is more severe at high gas flow. This fact could be ascribed to the gas flow through both the carbon matrix and the channels which is affected by the gas flow rate. As it was pointed out in the monolith characterization section, the carbon matrix is composed by highly opened macroporosity (several ten of micras) where the active phase is also deposited. Thus, the gas could flow through both this opened porosity and/or the channels. However, the pathway followed by the gases depends on the flow rate. At low flow rates, gas easily traverses both the channels and the broad porosity of the carbon skeleton in all monoliths, mitigating the impact of channel design in the catalytic activity. However, with an increase in flow rate a predominant portion of the gas

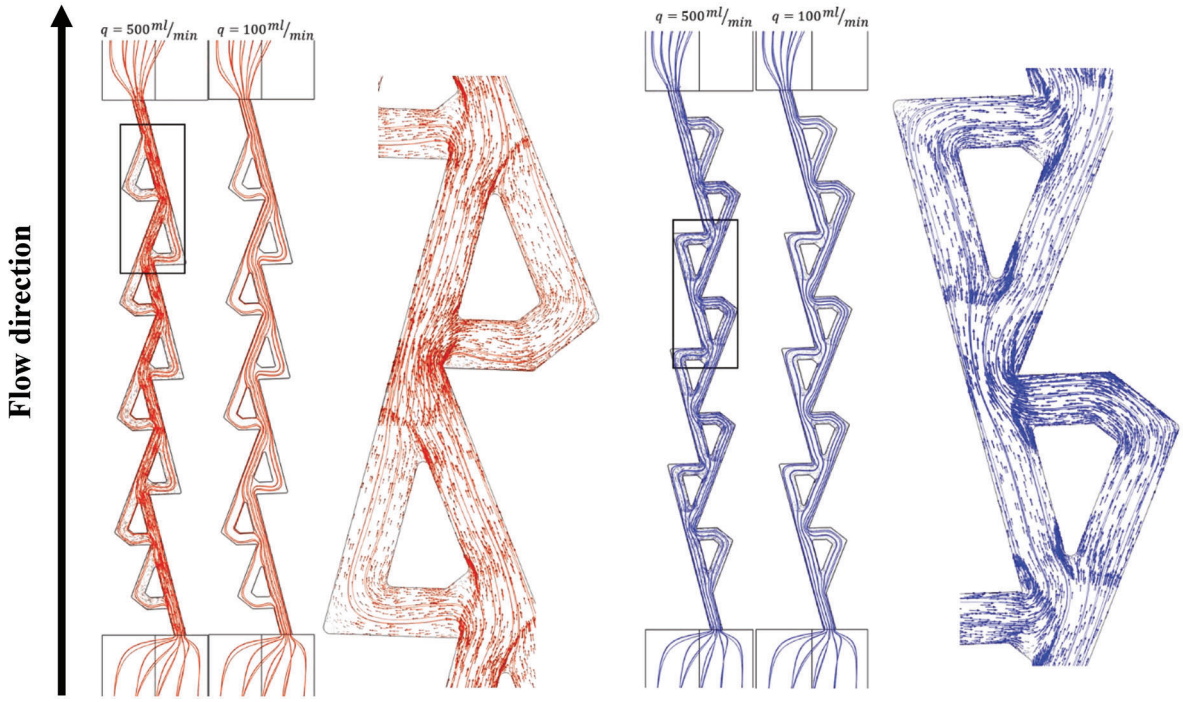

Figure 17. Streamlines of the reactive gaseous mixture inside one channel of the Tesla monolith, varying the gas flow rate and flow direction.

is compelled to flow through the channels, resulting in a more severe impact of the channel architecture.

In order to analyze in more detail, the effect of mass flow on the reaction rate, catalytic tests at different flow rates were performed and the reaction rate normalized by weight of Ni/CeO_2 is plotted in **Figure 10** for the three studied designs. A heterogeneous catalytic reaction can work under two regimens: diffusional control in which the reaction rate is controlled by the diffusion of reagents and products between the fluid bulk and the catalyst surface, or under chemical control in which the reaction rate is controlled by the kinetics of the chemical reaction. Under diffusional control, high volumetric flows augment the swift delivery of reactants and simultaneous removal of products thereby favoring the chemical reaction rate, so it relies on gas flow and, consequently, on the design of the monolith. On the other hand, in the chemical control of the reaction rate, the effectiveness of the catalyst's active phase is pivotal. Figure 10c shows that the reaction rate in C monolith increases by increasing the flow from 100 to 300 mL min^{-1}, indicating that the monolith with conventional straight channel design consistently operates under diffusional control. Note that at flows higher than 300 mL min^{-1}, the reaction rate declines with further increases in flow. This decline is attributed, as mentioned earlier, to the forced flow through straight channels, resulting in the loss of accessible active phase for catalytic reactions. In contrast, in monoliths with Tesla-valve type design (T and Tm), the reaction rate is not highly affected by the flow rate, denoting that they work under chemical control, at least up to 240 °C. It is important to highlight that again the modified Tesla-valve design (Tm) presents a better performance than that of the Tesla-valve (T). The Tm monolith works under chemical control at all the flows tested and the reaction rate is almost 30% higher than for the T monolith. This suggests that the presence of the tortuous Tesla-valve channels, mainly in Tm monolith, enhances the availability of active sites for facilitating chemical reactions. This effect is supported by the streamlines of fluid computed by numerical simulations in the following section.

However, the Tesla-valve channel architecture has a special configuration so that the fluid flows in different way in one direction or the other of the monolith (**Figure 11**). In the blocked direction (Figure 11a), part of the fluid seems "to rotate" (red) and interferes with the forward flow (black) in each stage. However, this does not occur in the opposite direction (Figure 11b) where the gas flows unobstructed. Thus, in the blocked direction local increases in pressure may arise due to the obstruction and convergence of flows, whereas it does not happen in the opposite direction. To analyze the benefits of the creation of these multistage auto-pressurized local microreactors on the catalytic performance, the Tm and T monoliths were tested in both directions at a flow of 500 mL min^{-1} to enhance a preferential flow through the channel rather than through the carbon matrix. The CO_2 conversion and the reaction rate are included in **Figure 12**.

In both Tesla-valve monoliths, the catalytic performance is enhanced in the blocked direction due to the fluid backmixing and the local multistage auto-pressurized microreactors created by this mixing which, according to Le Chatelier's principle, shifts the equilibrium to the CH_4 production. Note also, that the catalytic performance (CO_2 conversion and reaction rate) is, as commented above, improved in the Tm monolith regarding the T one due to the modification of the fluid dynamic caused by the change of the Tesla-valve angle. But this improvement, as expected, is observed in the blocked direction but not in the unimpeded direction. In the

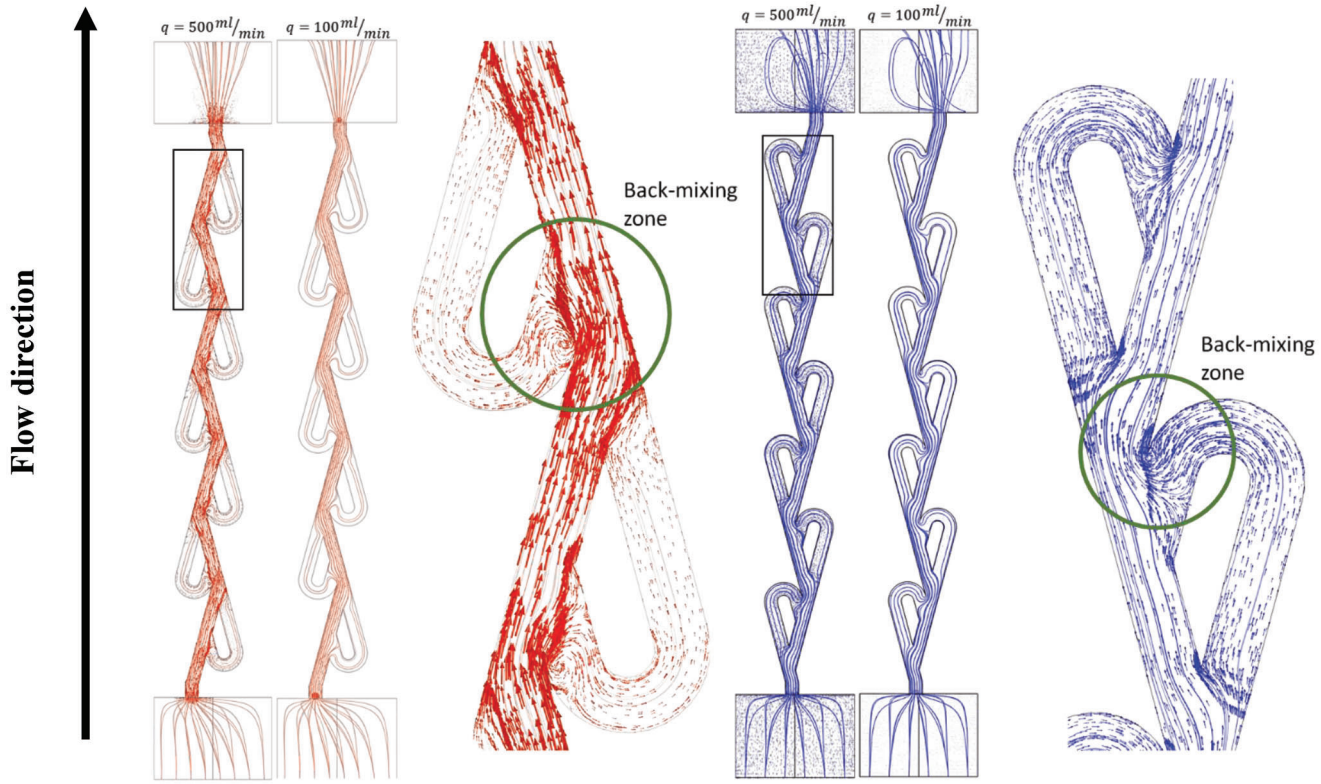

Figure 18. Streamlines of the reactive gaseous mixture inside one channel of the modified Tesla monolith, varying the gas flow rate and flow direction. The green circles identify the back mixing zones as depicted by arrows getting back.

latter, the gas does not pass through the Tesla bifurcation so, the flow path is the same in both Tesla monoliths showing a similar catalytic performance. Therefore, the improvement of curved angle is only observed in the blocked direction, where the flow bifurcates and converges through the Tesla-valve stages.

3.3. Fluid Dynamics Study

The mathematical model presented in Section 2.4 was numerically solved to compute the gas velocity and pressure inside the channels of the Tesla monoliths. With this objective, the software Comsol Multiphysics was used, which is based on the finite element method to convert the system of partial differential equations in a set of unknown primary variables in multiple subdomains discretizing the channels of the Tesla monoliths. Due to the repeatability of the channels that make up the Tesla monoliths, it is enough to solve the governing equations in a unique channel, by using the appropriate volumetric gas flow for just one channel. **Figure 13** presents the CAD design of the Tesla monoliths in the environment of the software Comsol Multiphysics. Once the geometry is available in Comsol, it is discretized into multiple subdomains (tetrahedra and pyramids) composing the grid mesh where primary unknowns (pressure, velocity in each direction, kinetic energy, and the rate of dissipation of kinetic energy) are computed by using iterative numerical methods. Comsol Multiphysics includes powerful algorithms to develop the grid mesh and solve the primary unknowns, and, in this work, we have employed the default configuration of such algorithms. Observe in **Figure 14** how sharp corners induce the generation of thousands of subdomains, increasing noticeably the number of subdomain elements for the case of the Tesla monolith, while for the modified Tesla monolith the existence of round lobes needs much fewer subdomains. Despite such differences, care was taken that the computed pressure and velocity do not depend on the number of domain elements.

Figures 15 and **16** present the gas fluid velocity for the Tesla and modified Tesla monoliths, correspondingly. There are appreciable differences in the magnitude and preferential directions of the reactive gaseous mixture flowing through the catalytic monoliths. On the one hand, the modified Tesla design yields a major contrast between the velocity reached by the fluid in the central channel in comparison with the fluid velocity in the adjacent lobes (look at the contrast of the color legends). In simple words, it seems the appearance of "stagnant fluid" in the lobes surrounding the main flow channel. This effect is not observed in the Tesla monolith, where the angle of the entrance to the lobes yields a "more uniform" spatial distribution of the gas velocity through the entire monolith, of course, in comparison with the modified Tesla. This phenomenon, undoubtedly, affects the rate of providing reactants and removing products from the lobes surrounding the central channel of the monolith.

The flow patterns were investigated in both monolith designs by varying the flow direction and volumetric flow rate. In

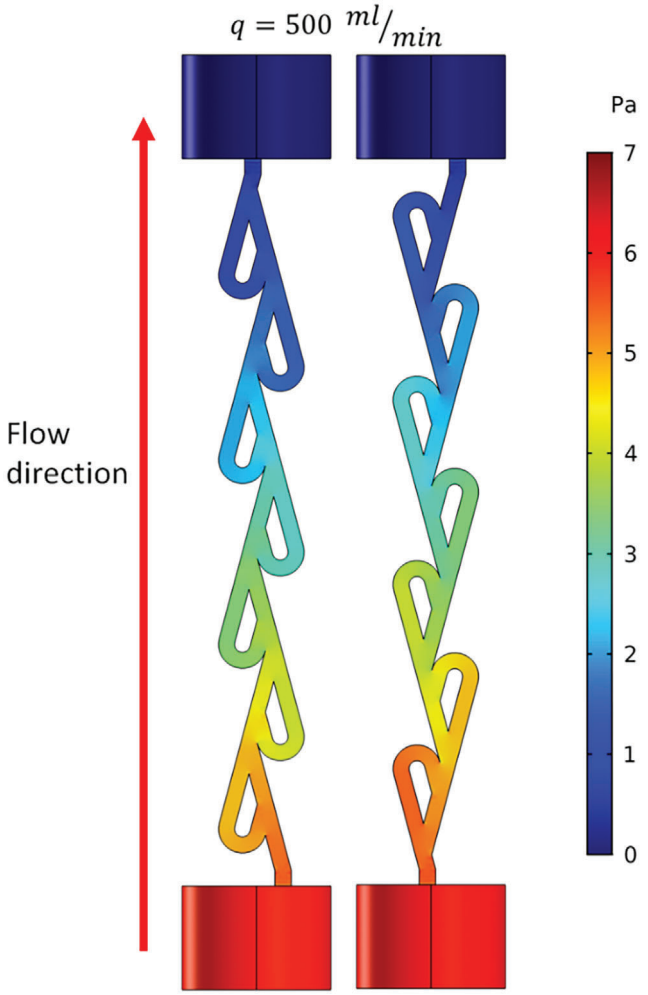

Figure 19. Fluid pressure profile inside the modified Tesla monolith. Here the pressure subtracted by the atmospheric pressure (gauge pressure).

Figure 17 there are plotted streamlines corresponding to the Tesla monolith, while the analogous graphics for the modified Tesla monolith are presented in **Figure 18**. There are notorious differences appreciated in the flow patterns between both Tesla monoliths. The quantity of stagnant fluid is larger when the blocking phenomenon takes place, according to the explanation of Figure 11, and this phenomenon is more significant in the modified Tesla (note the quantities and length of the velocity vectors, arrows, between the central region and those in the surrounding lobes). Such a feature is not notoriously observed in the case of the Tesla monolith. The case of the monolith with angled lobes provides conditions for a major entrance of fluid with larger velocity and, furthermore, decreases slightly the fluid pressure. As observed further, this variation of pressure explains why the modified Tesla operating under blocking flow configuration yields better reaction conditions for CO_2 consumption. In Figure 18 we have identified in green circles those zones where the gas performs back-mixing just when the fluid is incorporated from the lateral lobe into the central channel. Besides, observe how the back-mixing conditions are more notorious in the modified Tesla in comparison with the Tesla monolith. Eventually, as demonstrated by the experimental chemical reaction results, the existence of retro-mixing positively favors the CO_2 conversion.

Another variable that may be influencing the rate of chemical reactions is the concentration of solutes. As we are dealing with a gaseous mixture, the molar concentrations of all the chemical components depend on the local pressure and temperature. In our simulations, we found a "practically linear" variation of the fluid pressure along the monolith as observed in the results plotted in **Figure 19**. However, a thorough inspection allows us to observe slightly major pressures in the lobes of the monolith corresponding to the blocked direction configuration (see Figure 11), this will lead to larger solute concentrations with further improvement in the chemical reaction rates. Finally, we have also plotted the level curves of pressure for each monolith, as one alternative to highlight the local variations of the fluid pressure (**Figure 20**). In this type of graphic, isolated concentrated level curves indicate the existence of strong pressure gradients in one small region. In this sense, strong local pressure gradients are observed more clearly in the modified Tesla monolith. Such pressure behavior agrees well with the generation of a "more uniform" fluid velocity in the surrounding lobes (see the green ellipses in Figure 20). In turn, the existence of uniform pressure zones favors higher concentrations of solutes.

4. Conclusion

The combination of the sol–gel polymerization and 3D printing technology allows to obtain monolithic catalysts with specifically controlled channels designs which has opened the gate to obtain advanced functional materials for many industrial applications. A new concept is developed in this work, auto-pressurized multistage Tesla-valve type monolithic microreactors where not only the fluid dynamics and thus, the active phase-reactants contact

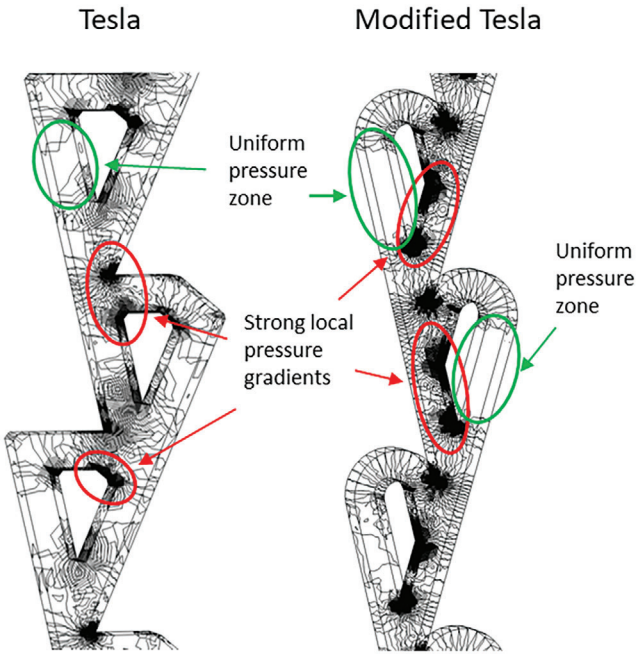

Figure 20. Level curves of the fluid pressure inside the Tesla monoliths.

is perfectly controlled and optimized but also local reaction conditions such as pressure is controlled to enhance the reaction kinetic. For that, carbon monoliths featuring Tesla-like channel shapes (referred to as T and Tm) were created using a combination of 3D printing and the sol–gel process and compared with a conventional honeycomb monolith. These monoliths were further utilized as supports for Ni/CeO_2 catalysts in the methanation of CO_2, a significant method for both CO_2 utilization and environmental remediation. Furthermore, a mathematical model incorporating momentum balance was developed to analyze velocity profiles and pressure drops in the monolithic structures. Experimental data and mathematical simulations confirmed the enhanced performance achieved with the complex design compared to conventional one. The irregular flow patterns induced by changes in flow direction, along with local pressure increases resulting from flow convergence, potentially enhance the Sabatier reaction in accordance with Le Châtelier's principle.

Unlike straight channels, the T and Tm designs exhibited consistent performance regardless of flow rate and demonstrated chemical control, particularly up to temperatures of 240 °C. Additionally, the Tm configuration, featuring curved angles, improved mass transfer, leading to higher conversion rates and ≈30% increase in reaction rate compared to the T configuration.

In conclusion, this auto-pressurized multi-stage Tesla-valve monolith opens up possibilities for designing specific and advanced functional materials for various chemical reactions. It not only maximizes contact between reactants and active phases but also enables control over reaction conditions to optimize reaction kinetics.

Supporting Information

Supporting Information is available from the Wiley Online Library or from the author.

Acknowledgements

This research had been supported by the Spanish project PID2021-127803OB-I00 funded by MCIN/AEI/ 10.13039/501100011033/ and by "ERDF A way of making Europe". Authors also thanks the "Unidad de Excelencia Química Aplicada a Biomedicina y Medioambiente" of the University of Granada (UEQ – UGR) for its technical assistance. A. Parra-Marfil appreciates the financial support provided by CONAHCYT through the PhD grant 818974. E. Bailón-García was grateful to MICINN for her postdoctoral fellowship (RYC2020-029301-I). A. Bueno López thanks the financial support of Generalitat Valenciana (Project CIPROM/2021/74).

Conflict of Interest

The authors declare no conflict of interest.

Data Availability Statement

The data that support the findings of this study are available from the corresponding author upon reasonable request.

Keywords

additive manufacturing, auto-pressurized monolithic catalyst, CO_2 capitalization, CO_2 methanation reaction, fluid dynamics, mathematical modeling, Tesla-valve configuration

Received: February 29, 2024
Revised: April 22, 2024
Published online:

[1] A. Modak, P. Bhanja, S. Dutta, B. Chowdhury, A. Bhaumik, *Green Chem.* **2020**, *22*, 4002.
[2] Y. Wang, S. Jeong, Y. Hang, Q. Wang, *Environ. Impact Assess. Rev.* **2022**, *98*, 106979.
[3] M. A. Zambrano-Monserrate, *Sci. Total Environ.* **2023**, *907*, 167852.
[4] M. C. Bacariza, D. Spataru, L. Karam, J. M. Lopes, C. Henriques, *Processes* **2020**, *8*, 1646.
[5] S. Biswas, C. Kundu, W. Lin Ng, S. Priya Samudrala, T. Jarvis, S. Giddey, S. Bhattacharya, *J. CO2 Util.* **2023**, *72*, 102501.
[6] W. Huang, J. Dai, L. Xiong, *Sustain. Energy Technol. Assessments* **2022**, *52*, 102059.
[7] G. Jabotra, P. K. Yadav, S. Kumar, S. Shama, *J. Mol. Catal.* **2019**, *547*, 113365.
[8] R. Steinberger-Wilckens, B. Sampson, in *Science and Engineering of Hydrogen-Based Energy Technologies: Hydrogen Production and Practical Applications in Energy Generation* (Eds: P.E. Miranda), Academic Press, Cambridge, Massachusetts **2019**.
[9] P. Styring, S. McCord, S. Rackley, in *Negative Emissions Technologies for Climate Change Mitigation* (Eds: S. Rackley, T. Ming, W. Li, M. Tyka, A. Sewel, D. Clery, G. Dowson, P. Styring, G. Andrews, S. McCord, P. Knops, R. de Richter), Elsevier Science, **2023**, 17.
[10] T. Yarbas, N. Ayas, *Int. J. Hydrogen Energy* **2023**, *49*, 1134.
[11] L. Di, Z. Fu, M. Dong, A. Zhu, G. Xia, X. Zhang, *Chem. Eng. Sci.* **2023**, *280*, 119056.
[12] L. Gómez, I. Martínez, V. Navarro, R. Murillo, *J. CO2 Util.* **2023**, *77*, 102611.
[13] Y. Xie, J. Wen, Z. Li, J. Chen, Q. Zhang, P. Ning, Y. Chen, J. Hao, *Green Chem.* **2023**, *25*, 130.
[14] I. Amez, S. Gonzalez, L. Sanchez-Martin, M. F. Ortega, B. Llamas, in *Climate Change Science: Causes, Effects and Solutions for Global Warming* (Eds: D. Ting, J. A. Stagner) Elsevier, **2021**, 5.
[15] S. Lin, R. Tang, X. Liu, L. Gong, Z. Li, *Int. J. Hydrogen Energy* **2024**, *51*, 462.
[16] Z. Li, T. Zhao, L. Zhang, *Appl. Organomet. Chem.* **2018**, *32*, e4328.
[17] A. I. Tsiotsias, N. D. Charisiou, C. Italiano, G. D. Ferrante, L. Pino, A. Vita, V. Sebastian, S. J. Hinder, M. A. Baker, A. Sharan, N. Singh, K. Polychronopoulou, M. A. Goula, *Appl. Surf. Sci.* **2024**, *646*, 158945.
[18] M. Mihet, M. D. Lazar, *Catal. Today* **2018**, *306*, 294.
[19] R.-Y. Chein, C.-C. Wang, *Catalysts* **2020**, *10*, 1112.
[20] A. Quindimil, U. De-La-Torre, B. Pereda-Ayo, A. Davó-Quiñonero, E. Bailón-García, D. Lozano-Castelló, J. A. González-Marcos, A. Bueno-López, J. R. González-Velasco, *Catal. Today* **2020**, *356*, 419.
[21] L. M. N. C. Alves, M. P. Almeida, M. Ayala, C. D. Watson, G. Jacobs, R. C. Rabelo-Neto, F. B. Noronha, L. V. Mattos, *Chem. Eng. Sci.* **2021**, *239*, 116604.
[22] A. Quindimil, M. C. Bacariza, J. A. González-Marcos, C. Henriques, J. R. González-Velasco, *Appl. Catal. B* **2021**, *296*, 120322.
[23] Y. Wei, J. Ji, F. Liang, D. Ma, Y. Du, Z. Pang, H. Wang, Q. Li, G. Shi, Z. Wang, *J. Environ. Chem. Eng.* **2023**, *11*, 110773.
[24] E. M. Mendoza-Núñez, J. C. Fierro-Gonzalez, T. A. Zepeda, A. Solis-Garcia, *Mol. Catal.* **2022**, *533*, 112801.
[25] K. Tamimi, S. M. Alavi, M. Rezaei, E. Akbari, *J. Energy Inst.* **2021**, *99*, 48.
[26] Y. Liao, Y. He, X. Cui, L. Liu, *Fuel* **2024**, *355*, 129494.
[27] T. Zhang, P. Zheng, F. Gu, W. Xu, W. Chen, T. Zhu, Y. F. Han, G. Xu, Z. Zhong, F. Su, *Appl. Catal. B* **2023**, *323*, 122190.
[28] W. J. Lee, C. Li, H. Prajitno, J. Yoo, J. Patel, Y. Yang, S. Lim, *Catal. Today* **2021**, *368*, 2.

[29] G. Varvoutis, A. Lampropoulos, P. Oikonomou, C. D. Andreouli, V. Stathopoulos, M. Lykaki, G. E. Marnellos, M. Konsolakis, *J. CO2 Util.* **2023**, *70*, 102425.
[30] M. Song, L. Shi, X. Xu, X. Du, Y. Chen, W. Zhuang, X. Tao, L. Sun, Y. Xu, *J. CO2 Util.* **2022**, *64*, 102150.
[31] M. Safdar, M. González-Castaño, A. Penkova, M. A. Centeno, J. A. Odriozola, H. Arellano-García, *Appl. Mater. Today* **2022**, *29*, 101577.
[32] J. Gao, Q. Liu, F. Gu, B. Liu, Z. Zhong, F. Su, *RSC Adv.* **2015**, *5*, 22759.
[33] H. T. T. Nguyen, Y. Kumabe, S. Ueda, K. Kan, M. Ohtani, K. Kobiro, *Appl. Catal. A Gen.* **2019**, *577*, 35.
[34] T. Zhang, W. Wang, F. Gu, W. Xu, J. Zhang, Z. Li, T. Zhu, G. Xu, Z. Zhong, F. Su, *Appl. Catal. B* **2022**, *312*, 121385.
[35] F. Hu, C. Jin, R. Wu, C. Li, G. Song, T. Z. H. Gani, K. H. Lim, W. Guo, T. Wang, S. Ding, R. Ye, Z. H. Lu, G. Feng, R. Zhang, S. Kawi, *Chem. Eng. J.* **2023**, *461*, 142108.
[36] M. Seemann, H. Thunman, in *Substitute Natural Gas from Waste: Technical Assessment and Industrial Applications of Biochemical and Thermochemical Processes* (Eds: M. Materazzi, P.U. Foscolo) Academic Press, **2019**, Ch. 9.
[37] R. Chava, A. V. D. Bhaskar, B. Roy, S. Appari, *Mater. Today Proc* **2023**, *72*, 134.
[38] H. Y. Chen, J. Pihl, T. J. Toops, S. Sinha Majumdar, *Appl. Catal. A Gen.* **2023**, *656*, 119140.
[39] N. Majidian, S. Soltanali, *J. Jpn. Pet. Inst.* **2016**, *59*, 126.
[40] S. Roy, A. K. Heibel, W. Liu, T. Boger, *Chem. Eng. Sci.* **2004**, *59*, 957.
[41] S. Danaci, L. Protasova, J. Lefevere, L. Bedel, R. Guilet, P. Marty, *Catal. Today* **2016**, *273*, 234.
[42] C. Fukuhara, K. Hayakawa, Y. Suzuki, W. Kawasaki, R. Watanabe, *Appl. Catal. A Gen.* **2017**, *532*, 12.
[43] A. Vita, C. Italiano, L. Pino, P. Frontera, M. Ferraro, V. Antonucci, *Appl. Catal. B* **2018**, *226*, 384.
[44] F. Agueniou, H. Vidal, J. de Dios López, J. C. Hernández-Garrido, M. A. Cauqui, F. J. Botana, J. J. Calvino, V. V. Galvita, J. M. Gatica, *Catal. Commun.* **2021**, *148*, 106181.
[45] H. L. Huynh, W. M. Tucho, Z. Yu, *Green Energy Environ.* **2020**, *5*, 423.
[46] G. Groppi, E. Tronconi, P. Forzatti, *Catal. Today* **1993**, *17*, 237.
[47] C. Y. Chaparro-Garnica, E. Bailón-García, A. Davó-Quiñonero, D. Lozano-Castelló, A. Bueno-López, *Chem. Eng. J.* **2022**, *432*, 134218.
[48] A. Davó-Quiñonero, D. Sorolla-Rosario, E. Bailón-García, D. Lozano-Castelló, A. Bueno-López, *J. Hazard Mater.* **2019**, *368*, 638.
[49] M. González-Castaño, F. Baena-Moreno, J. Carlos Navarro de Miguel, K. U. M. Miah, F. Arroyo-Torralvo, R. Ossenbrink, J. A. Odriozola, W. Benzinger, A. Hensel, A. Wenka, H. Arellano-García, *Energy Convers. Manag.* **2022**, *258*, 115464.
[50] C. Y. Chaparro-Garnica, E. Bailón-García, D. Lozano-Castelló, A. Bueno-López, *Catal. Sci. Technol.* **2021**, *11*, 6490.
[51] Q. Wei, H. Li, G. Liu, Y. He, Y. Wang, Y. E. Tan, D. Wang, X. Peng, G. Yang, N. Tsubaki, *Nat. Commun.* **2020**, *11*, 4098.
[52] J. Lefevere, S. Mullens, V. Meynen, *Chem. Eng. J.* **2018**, *349*, 260.
[53] C. Y. Chaparro-Garnica, A. Davó-Quiñonero, E. Bailón-García, D. Lozano-Castelló, A. Bueno-López, *ACS Appl. Mater. Interfaces* **2019**, *11*, 36763.
[54] A. Cárdenas-Arenas, H. Soriano Cortés, E. Bailón-García, A. Davó-Quiñonero, D. Lozano-Castelló, A. Bueno-López, *Fuel Process. Technol.* **2021**, *212*, 106637.
[55] S. You, S. Xing, C. Jiang, *Mater. Charact.* **2023**, *205*, 113327.
[56] J. Ma, N. Xu, Y. Luo, Q. Liu, Y. Pu, *Ceram. Int.* **2023**, *49*, 4929.
[57] K. Q. Liu, C. B. Wu, W. Q. Kang, *Opt. Mater. (Amst)* **2024**, *148*, 114840.
[58] F. Lang, D. Sun, J. Liu, H. Wang, H. Yan, *Mater. Lett.* **2016**, *181*, 328.
[59] J. Serafin, J. Llorca, *Molecules* **2023**, *28*, 2926.
[60] S. Loridant, *Catal. Today* **2021**, *373*, 98.
[61] N. Kainbayev, M. Sriubas, D. Virbukas, Z. Rutkuniene, K. Bockute, S. Bolegenova, G. Laukaitis, *Coatings* **2020**, *10*, 432.
[62] B. Sellers-Antón, E. Bailón-García, A. Cárdenas-Arenas, A. Davó-Quiñonero, D. Lozano-Castelló, A. Bueno-López, *Environ. Sci. Technol.* **2020**, *54*, 2439.
[63] A. Cárdenas-Arenas, A. Quindimil, A. Davó-Quiñonero, E. Bailón-García, D. Lozano-Castelló, U. De-La-Torre, B. Pereda-Ayo, J. A. González-Marcos, J. R. González-Velasco, A. Bueno-López, *Appl. Mater. Today* **2020**, *19*, 100591.
[64] E. Bailón-García, F. Carrasco-Marín, A. F. Pérez-Cadenas, F. J. Maldonado-Hódar, *Catal. Commun.* **2016**, *82*, 36.
[65] K. Miura, J. Hayashi, K. Hashimoto, *Carbon* **1991**, *29*, 653.
[66] H. Guo, S. Tian, L. Wang, C. Xiao, S. Yang, *Int. J. Hydrogen Energy* **2024**, *50*, 1573.
[67] J.-Y. Qian, M.-R. Chen, Z.-X. Gao, Z.-J. Jin, *Energy* **2019**, *179*, 647.
[68] Y. Bao, H. Wang, *Int. J. Heat Mass Transf.* **2022**, *187*, 122540.
[69] K. Monika, C. Chakraborty, S. Roy, R. Sujith, S. P. Datta, *Int. J. Heat Mass Transf.* **2021**, *177*, 121560.
[70] A. R. Gamboa, C. J. Morris, F. K. Forster, *J. Fluids Eng.* **2004**, *127*, 339.
[71] S. M. Thompson, B. J. Paudel, T. Jamal, D. K. Walters, *J. Fluids Eng.* **2014**, *136*, 081102.
[72] P. R. Porwal, S. M. Thompson, D. K. Walters, T. Jamal, *Numer. Heat Transf. A Appl.* **2018**, *73*, 347.
[73] S. I. Martinez-Monteagudo, K. Rathnakumar, *Innov. Food Processing Technol.: A Comprehen. Rev.* **2021**, *19*.
[74] R. Sehrawat, B. P. Kaur, P. K. Nema, S. Tewari, L. Kumar, *Food Sci. Biotechnol.* **2021**, *30*, 19.
[75] H. Hu, V. M. Balasubramaniam, *Encyclopedia of Food Safety* **2024**, 531.